

# High-frequency Resonances of Train-track Coupled System due to Multiple Wheels Interference

Yaojun Ge\*

*State Key Laboratory of Disaster Reduction in Civil Engineering, Tongji University, 1239 Siping Road,  
Shanghai, 200092, China  
yaojunge@tongji.edu.cn*

Simian Lei

*State Key Laboratory of Disaster Reduction in Civil Engineering, Tongji University, 1239 Siping Road,  
Shanghai, 200092, China  
1810723@tongji.edu.cn*

Qi Li

*Department of Bridge Engineering, Tongji University, 1239 Siping Road,  
Shanghai, 200092, China  
liqi\_bridge@tongji.edu.cn*

A significant resonance pattern at high frequencies around 400 Hz to 1000 Hz has been well observed from measured rail accelerations. Such resonances are key issues for rail noise and corrugation. Although this pattern has been noted and discussed in various papers in terms of wave reflections among multiple wheels, the aim of this study is to develop novel dynamic model and reveal generation mechanism of this resonance phenomenon with the train-track coupled system. An infinite Timoshenko beam with continuous supports is adopted for modelling the track system, and the point and transfer receptances of the rail for a moving excitation are explicitly deduced by the residue theorem together with a Fourier transform-based method. A frequency-domain method is then established to calculate the power spectral densities (PSD) of the train-track coupled system responses to stochastic irregularities with the moving vehicle model with multiple wheels. It is found that the high-frequency resonances occur when the reflected waves generated from multiple wheels on the rail are exactly in phase with the initial track irregularity. The load speed has negligible influence on the wheel-rail interaction in the lower frequency range and a small influence in the upper frequency range only for very high train speeds.

**Keywords:** High-frequency resonance; infinite Timoshenko beam; point receptance; train-track couple system; multi-wheel moving excitation; track irregularity.

## 1. Introduction

High-frequency resonance around 400 Hz to 1000 Hz has been well observed from field measurement of rail accelerations, which are key issues for rail noise and corrugation.[1-3] Various studies found this resonance phenomenon can be attributed to the wheel-rail interactions between irregular profiles on wheels and rail contact surfaces and the vibration

\* Corresponding author, E-mail address: [yaojunge@tongji.edu.cn](mailto:yaojunge@tongji.edu.cn) (Y. Ge).

This is the accepted manuscript version of the article.

The final published version of this article is available at <https://doi.org/10.1142/S0219455423400187>

© 2025. Licensed under the CC-BY-NC-ND 4.0 license <https://creativecommons.org/licenses/by-nc-nd/4.0/>

induced by multiple wheel moving on the rail with interference.[4-6] The key to the question is how to develop high-precision dynamic model [7, 8] and reveal intrinsic generation mechanism of this resonance in train-track coupled system.[9]

Wheel-rail interactions generated in the railway system are primarily caused by irregular profiles on the wheel and rail contact surfaces, among which the general track geometry irregularities are the main source. It is found the responses of the train-track coupled system induced by track irregularities may present a series of peaks in the spectra at different frequencies associated with various mechanisms.[10, 11] These peaks may lead to higher ambient noise at specific frequencies up to thousands of Hertz,[12, 13] negatively influencing the comfort of passengers and residential areas with trains passing by. Moreover, the dominant wheel-rail contact forces generated in high frequencies prove crucial in the process of railhead corrugation,[14] leading to increased interactions in turn. In view of these detrimental effects, a great many attempts have been made to investigate the generation mechanism of these peaks in the vibrations of train-track system and wheel-rail interaction forces.

Due to the effects of multiple wheels on a rail, the vibration induced by multiple wheel-rail interactions is observed to display more peaks than that of a single wheel-rail interaction.[15] In an earlier study by Igeland [14] a series of peaks around 600-800 Hz were found in the spectra of wheel-rail contact forces in the model of a bogie running on a discretely supported rail. Wu and Thompson [10] firstly brought forward the concepts of active wheel and passive wheel for evaluating the track response excited by multiple wheels. An interesting peak around 600 Hz was then observed in the active wheel-rail interaction force as well as in the point receptance of a rail with additional passive wheels attached.[10, 16] Wu and Thompson [17] then developed forward this research and studied these peaks in detail by using a track model with multiple wheels attached. Unlike the results from a single-wheel model, four main peaks were shown to appear in the spectra of contact forces around 550-1200 Hz. In order to explain these additional peaks, the influence of wave reflections between multiple wheels was qualitatively studied. Such cases also happened to Ding et al.[18] when investigating the effects of wave reflections between multiple wheels on curve squeal.

The primary step in studying these resonances is to evaluate the point receptance of the rail, which is crucial in dealing with wheel-rail interactions either in the time domain or frequency domain.[19] An infinite Timoshenko beam on discrete supports is often adopted to consider the effect of shear deformation and rotation inertia of the rail at frequencies above 500 Hz [20]. Sheng et al.[21] developed a wavenumber-based method in order to calculate the response of the track to a harmonic load of high frequency and moving at high speed. Notice that the point receptance of such a discretely supported model is not completely harmonic, raising troubles in analyzing train-track dynamics in the frequency domain.[21, 22] However, the discreteness effect can be disregarded if the interested frequency does not fall in the vicinity of the pinned-pinned resonance.[23] With a continuously supported model, the track becomes a linear time invariant system and gives a stationary response with a certain frequency in the moving frame when subjected to a

moving harmonic load.[24] It should be mentioned that a moving excitation model [10, 16, 17, 25] is often applied to calculate wheel-rail interactions, in which wheels are regarded as stationary and irregularities are strapped between the wheels and the rail as a relative excitation.[17] Unlike the moving wheel model, the effect of load motion on the rail receptance is not considered in such a moving roughness model.[26] This effect on the point receptance of an Euler-Bernoulli beam was later discussed by Thompson,[27] showing that the wavelength ahead of the load is shorter than that behind the load.

Recently, peaks around the frequencies of 400 Hz to 1000 Hz in track vibrations have been once more observed during several field measurements made on an elevated railway with ballastless track. Although this phenomenon has been revisited in several papers, it still needs quantitative phase analyses and detailed demonstrations of wave interference process. The aim of this study is to theoretically investigate the generation mechanism of this phenomenon both from mathematical and physical points of view. A typical model of an infinite Timoshenko beam with continuous supports is adopted to model the track system, and its point and transfer receptances are explicitly derived by means of the Fourier transform-based method and the residue theorem. Then, the power spectral densities (PSDs) of the system response are analytically derived and expressed as three parts: the frequency response function (FRF) of the vehicle subsystem, the dynamic stiffness matrix of equivalent wheel-rail contact forces and the PSD for the track irregularities. Based on the concepts of active and passive wheels,[10] the multiple peaks in the PSDs of the wheel-rail interaction forces are investigated from a mathematical point of view by extreme value analysis of the response function and from a physical point of view based on the wave propagation theory. In the last section, the effect of load motion on the response of train-track coupled system is discussed, based on the model of four wheels running on a Timoshenko rail, considering the influence of different types of pad stiffness and train speed.

## 2. Field Measurement

A field measurement was made at an urban rail transit viaduct in Shanghai, China, where the track is supported by U-shaped girders, as shown in Fig. 1 (a). The nominal fastener stiffness is 40 MN/m in the vertical direction, with a fastener spacing of 0.6 m. The rail vibration was measured using a piezoelectric accelerometer mounted on the outboard rail foot shown schematically in Fig. 1 (b), with a sampling frequency of 10 kHz. Fig. 2 show the time history and a PSD estimate of the vertical acceleration of the rail during the passage of a three-vehicle train running at 60 km/h. The PSD is obtained by using Welch's method with overlapping time segments, resulting in a frequency resolution of 4.883 Hz.



Fig. 1. Photo of field test: (a) an urban rail transit viaduct in Shanghai; (b) piezoelectric accelerometer mounted on the outboard rail foot.

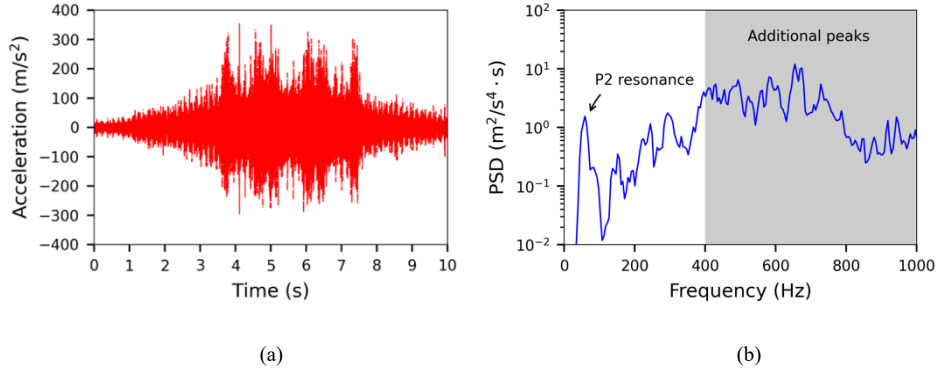


Fig. 2. Measured vertical accelerations of the rail from field test: (a) time history; (b) PSD.

As can be seen from Fig. 2 (b), in addition to random variations caused by the excitation due to the track irregularities, there are several peaks in the PSD which can be divided into two categories. In the low frequency region, a strong peak occurs at around 50 Hz that corresponds to the so-called P2 resonance of the wheel mass on the track stiffness.[27, 28] A peak at around 170 Hz corresponds to the resonance of the rail mass bouncing on the pad stiffness.[27] In the frequency range from 400 Hz to 1000 Hz, there are additional peaks which may be due to the presence of multiple wheels on the rail.[10, 16] The generation mechanism of these additional peaks is investigated in the following sections.

### 3. Point Receptance of Infinite Timoshenko Beam

The track is usually supported by periodic sleepers, yet the point receptance of it is not purely harmonic, causing difficulties in dealing with train-track dynamics in the frequency domain. In fact, the discreteness effect can be neglected if dominating frequencies don't fall in the vicinity of the pinned-pinned resonance,[20, 29] especially if the rail pads are relatively soft.[15, 30, 31] In addition, it was shown by Wu and Thompson [10] that the effects of multiple wheel-rail interactions may also suppress the pinned-pinned mode. As

the shear deformation and rotational inertia of the rail should be considered for frequencies over 500 Hz,[20] a continuously supported Timoshenko beam model subjected to a moving harmonic load [24] is used in this study to obtain the point and transfer receptances of the track in the moving frame of reference, initially without wheels mounted on it.

### 3.1. Track model

The vibration of a Timoshenko beam is described by the vertical displacement  $w_r$  (directed positive downwards) and the rotation angle  $\phi_r$  of the cross-section (clockwise), as shown in Fig. 3. For a harmonic load  $Qe^{i\omega_0 t}$  moving at a speed  $V$ , with amplitude  $Q$  and angular frequency  $\omega_0$ , the kinetic equations for an infinite Timoshenko beam with continuous supports [27] can be rewritten in the moving coordinate system attached to the load, i.e.,  $\xi = x - Vt$ ,

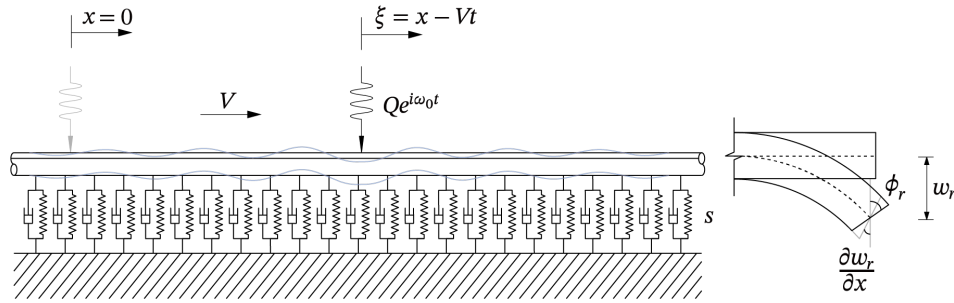


Fig. 3. An infinite Timoshenko beam on an elastic foundation showing the vibration generated by a moving harmonic load.

$$\begin{cases} GA\kappa \frac{\partial}{\partial \xi} \left( \phi_r - \frac{\partial w_r}{\partial \xi} \right) + s w_r + \rho A \left( \frac{\partial^2 w_r}{\partial t^2} + V^2 \frac{\partial^2 w_r}{\partial \xi^2} - 2V \frac{\partial^2 w_r}{\partial \xi \partial t} \right) = Q \delta(\xi) e^{i\omega_0 t} \\ GA\kappa \left( \phi_r - \frac{\partial w_r}{\partial \xi} \right) - EI \frac{\partial^2 \phi_r}{\partial \xi^2} + \rho I \left( \frac{\partial^2 \phi_r}{\partial t^2} + V^2 \frac{\partial^2 \phi_r}{\partial \xi^2} - 2V \frac{\partial^2 \phi_r}{\partial \xi \partial t} \right) = 0 \end{cases} \quad (1)$$

where  $\rho A$  is the rail mass per unit length,  $\rho I$  is the rail rotational inertia,  $EI$  is the rail bending stiffness,  $GA$  is the rail shear stiffness,  $\kappa$  is the rail shear parameter, and  $s$  is the support stiffness per unit length. Damping is introduced in the supports by making the stiffness complex with the form  $s(1 + i\eta)$  (this is suppressed in the equations for simplicity).

### 3.2. Solution based on Fourier-transform method

By taking a Fourier transform, Eq. (1) can be transformed from the spatial domain to the wavenumber domain

$$\begin{cases} -GA\kappa i k \Phi + [GA\kappa k^2 + s - \rho A(kV + \omega_0)^2] W = Q \\ GA\kappa i k W + [GA\kappa + EI k^2 - \rho I(kV + \omega_0)^2] \Phi = 0 \end{cases} \quad (2)$$

Solving Eq. (2) yields the complex amplitudes  $W$  and  $\Phi$ , and then, the response  $w_r(\xi, t)$  at position  $\xi$  and time  $t$  can be obtained by performing the inverse Fourier transform with respect to  $k$  and  $\omega$

$$w_r(\xi, t) = \frac{Q e^{i\omega_0 t}}{2\pi} \int_{-\infty}^{\infty} \frac{M(k)}{N(k)} e^{-ik\xi} dk \quad (3)$$

where

$$M(k) = GA\kappa + EIk^2 - \rho I(kV + \omega_0)^2 \quad (4)$$

$$N(k) = [GA\kappa k^2 + s - \rho A(kV + \omega_0)^2][GA\kappa + EIk^2 - \rho I(kV + \omega_0)^2] - G^2 A^2 \kappa^2 k^2 \quad (5)$$

It is worth pointing out that the dynamic response is stationary and harmonic if the observation point moves with the load. Therefore, the train-track coupled system retains the linear superposition characteristic and the frequency-domain method becomes possible.

### 3.3. Track receptance

The transfer receptance of the track at a distance  $\xi$  from the load can be then obtained as

$$H(\xi, \omega_0) = \frac{1}{2\pi} \int_{-\infty}^{\infty} \frac{M(k)}{N(k)} e^{-ik\xi} dk \quad (6)$$

The integral in Eq. (6) can be evaluated by using contour integration. For  $\xi \geq 0$ , the integral is equal to  $-2\pi i$  times the sum of the residues of the poles in the lower half plane, whereas for  $\xi < 0$ , the integral is equal to  $2\pi i$  times the sum of the residues of the poles in the upper half plane. Hence, the receptance is given by

$$H(\xi, \omega_0) = \begin{cases} -i \sum_{n=3}^4 \text{Res} \left[ \frac{M(z)}{N(z)} e^{-i\xi z}, k_n \right] = -i \left[ \frac{M(k_3) e^{-i\xi k_3}}{N'(k_3)} + \frac{M(k_4) e^{-i\xi k_4}}{N'(k_4)} \right] & (\xi \geq 0) \\ i \sum_{n=1}^2 \text{Res} \left[ \frac{M(z)}{N(z)} e^{-i\xi z}, k_n \right] = i \left[ \frac{M(k_1) e^{-i\xi k_1}}{N'(k_1)} + \frac{M(k_2) e^{-i\xi k_2}}{N'(k_2)} \right] & (\xi < 0) \end{cases} \quad (7)$$

where  $k_n$  are the zeros of  $N(k)$  and  $\text{Im}(k_{1,2}) > 0$ ,  $\text{Im}(k_{3,4}) < 0$ . To illustrate the contour integration, use is made of typical parameters given in Table 1 for the rail, which are also applied in the following analysis. It is noted that the support stiffness of  $s = 66.67 \text{ MN/m}^2$  corresponds to a vertical fastener stiffness of  $40 \text{ MN/m}$  at a fastener spacing of  $0.6 \text{ m}$ . Damping is introduced in the rail pads and the rail as listed in Table 1. Fig. 4 (a) shows the distribution of the four poles  $k_n$  on the complex plane, for load speeds ranging from  $0 \text{ m/s}$  to  $100 \text{ m/s}$  and a frequency of  $300 \text{ Hz}$ . The decay rates for the track waves corresponding to  $k_3$  and  $k_4$  at a load speed of  $40 \text{ m/s}$  are shown in Fig.4 (b).

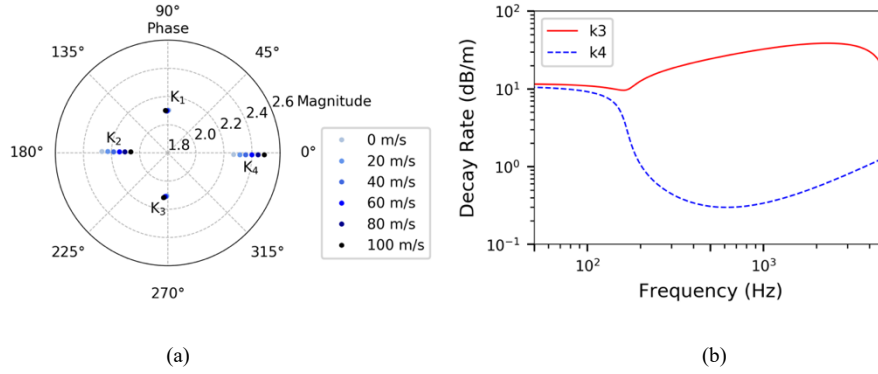


Fig. 4. Poles of  $N(k)$  on the complex plane and decay rates for the track waves using the parameters in Table 1: (a) distribution of four poles at a frequency of 300 Hz for various load speeds; (b) decay rates at a load speed of 40 m/s.

Table 1. Parameters for railway track based on Timoshenko beam model [27, 32]

Parameter	Definition	Unit	Value
$GA$	Rail shear stiffness	MN	617
$EI$	Rail bending stiffness	MNm <sup>2</sup>	6.42
$\eta_r$	Damping loss factor of rail	/	0.02
$\rho A$	Rail mass per unit length	kg/m	60
$\rho I$	Rail rotational inertia	Kgm	0.240
$\kappa$	Rail shear parameter	/	0.4
$s$	Support stiffness per unit length of foundation	MN/m <sup>2</sup>	66.67
$\eta_s$	Damping loss factor of foundation	/	0.15

As is shown in Fig. 4,  $k_2$  and  $k_4$  are the poles with the largest real part (positive or negative). The real part of the poles represents the wavenumber, and the imaginary part corresponds to decay with distance. It can be seen from Fig. 4 (b) that the decay rates for waves  $k_3$  and  $k_4$  both remain at a high level at frequencies below 200 Hz. However, at frequencies above 250 Hz, the rate of attenuation of the wave corresponding to the pole  $k_4$  is far lower than that of the pole  $k_3$ , indicating that the transfer receptance for the track at sufficient distance from the load is dominated by the  $k_4$  component at high frequencies.

The effect of the load speed on the poles is also shown in Fig. 4 (a). The pole  $k_4$  is related to the wave propagating in the same direction as the load speed and the pole  $k_2$  is related to the wave in the opposite direction. As the load speed increases, the poles  $k_2$  and  $k_4$  migrate slightly to the right, meaning that the wavelength for  $k_2$  wave increases and the wavelength for  $k_4$  wave decreases. This is the basis of the Doppler effect.[33] Fig. 5 (a) illustrates the effect of the load motion on the wave propagation along the rail, for a speed of 40 m/s and a frequency of 300 Hz. It is shown that the wave ahead of the load is compressed compared to the static case, whereas the wave behind the load is lengthened.

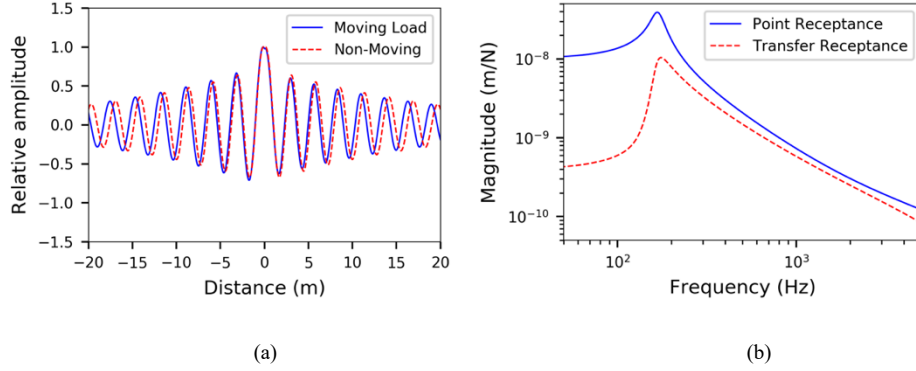


Fig. 5. The response of the rail: (a) instantaneous wave propagation along the rail at 300 Hz for a non-moving load and a load moving to the right with a speed of 40 m/s; (b) the point receptance and the transfer receptance magnitude at  $\xi = 2.5$  m for a load moving to the right at 40 m/s.

The point receptance of the rail and the transfer receptance at  $\xi = 2.5$  m for this case are also shown in Fig. 5 (b). It can be seen that magnitude of the transfer receptance is far lower than that of the point receptance at frequencies below 200 Hz, due to the high decay rates in this frequency region. A peak is found at around 200 Hz in both point and transfer receptances, corresponding to the resonance of the rail mass vibrating on the pad stiffness.[27]

#### 4. Dynamics of Train-track Coupled System

In this section, the receptances obtained in Section 3 are employed to derive the spectral density matrices for the response of the track and the vehicle (see Fig. 6) excited by random roughness or irregularities.

##### 4.1. Train-track coupled model

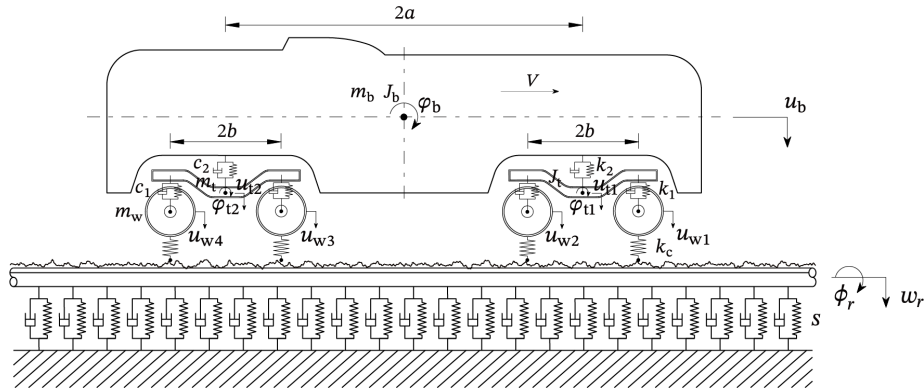


Fig. 6. Two-dimensional model of a half railway vehicle supported by an infinite elastic track represented by a Timoshenko beam.



The vehicle is assumed to be symmetric about the track centreline. It is represented by a half vehicle model consisting of a half car body, two half bogie frames, four wheels and several flexible spring-damper elements connecting them. The car body, bogie frames, and wheels are regarded as rigid bodies, and only vibration in the vertical direction is considered.[7] It is noted that, for vertical motion, the rigid model for the wheel is reasonable for frequencies below 1 kHz. At higher frequencies flexible modes in the radial direction occurring above 2 kHz should be considered.[27] Considering the natural frequencies of bridges are much lower than that of the wheel bouncing on the track, and the frequencies of the peaks of interest in this study are rather high, therefore the bridge structure is disregarded in the model, and this will have little effect on the stochastic response of the vehicle apart from its mean response. [34] Table 2 lists the definitions of the main parameters used to describe a half vehicle along with their values that relate to a metro train in Shanghai.

Table 2. Parameters for a metro used in urban rail transit viaduct in Shanghai

Parameter	Definition	Unit	Value
$m_b$	Mass of the half car body	Kg	$2.045 \times 10^4$
$J_b$	Pitch moment of inertia for the half car body	$\text{kg} \cdot \text{m}^2$	$8.994 \times 10^5$
$m_t$	Mass of the half bogie frame	Kg	$2.223 \times 10^3$
$J_t$	Pitch moment of inertia for the half bogie frame	$\text{kg} \cdot \text{m}^2$	$1.629 \times 10^3$
$m_w$	Mass of the wheel	Kg	$8.94 \times 10^2$
$a$	Half distance between the secondary suspensions	M	7.85
$b$	Half distance between the two wheels of each bogie	M	1.25
$k_1$	Vertical stiffness of the primary suspension per wheel	N/m	$1.22 \times 10^6$
$c_1$	Vertical damping of the primary suspension per wheel	$\text{N} \cdot \text{s/m}$	$1.5 \times 10^4$
$k_2$	Vertical stiffness of the secondary suspension per bogie	N/m	$3.4 \times 10^5$
$c_2$	Vertical damping of the secondary suspension per bogie	$\text{N} \cdot \text{s/m}$	$2.0 \times 10^4$
$k_c$	Equivalent vertical stiffness of wheel-track contact per wheel	N/m	$1.5 \times 10^9$

Based on the aforementioned assumptions, the vehicle model has a total of 10 degrees of freedom (DOFs), including seven translational and three rotational DOFs. The equation of motion for the vehicle subsystem can be expressed as

$$\mathbf{m}\ddot{\mathbf{u}} + \mathbf{c}\dot{\mathbf{u}} + \mathbf{k}\mathbf{u} = -\mathbf{f} \quad (8)$$

where  $\mathbf{m}$ ,  $\mathbf{c}$ , and  $\mathbf{k}$  are the mass, damping, and stiffness matrices for the vehicle, respectively.  $\mathbf{u}$  is the displacement vector of the vehicle.  $\mathbf{f}$  is the vector of the wheel-rail interaction forces. The negative sign in Eq. (8) represents the fact that the forces act upward on the wheels.

The wheel-rail contact model is an essential element for analyzing the dynamic performance of the entire system. A linearized contact spring is adopted to simplify the system as a linear stationary stochastic vibration problem (see Fig. 7), which is reasonable for typical levels of excitation. Thus, the interaction forces can be determined by

$$f_i = k_c u_{ci} \quad (9)$$

where  $u_{ci}$  is the relative compression across the  $i$ -th contact spring ( $i = 1, 2, 3, 4$ ) and  $k_c$  is the linearized contact stiffness.

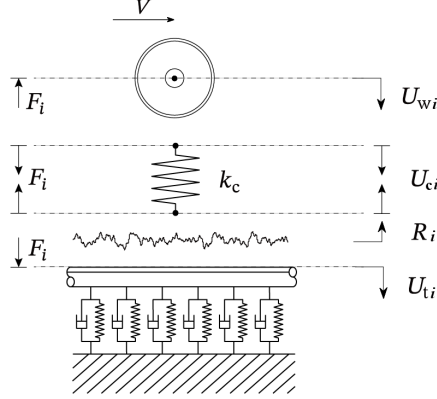


Fig. 7. Schematic diagram for mechanical analysis of the decomposed wheel-rail system.

Only vertical track irregularities are taken into consideration in this study. These are expressed by the US FRA vertical alignment irregularity PSD function  $S_r(\Omega)$  [35]

$$S_r(\Omega) = \frac{k A_r \Omega_c^2}{\Omega^2 (\Omega^2 + \Omega_c^2)} \quad (10)$$

where  $\Omega$  represents the spatial angular frequency of track irregularities;  $k$  represents the safety factor, which ranges from 0.25 to 1.0;  $A_r$  represents the roughness constant;  $\Omega_c$  represents the cutoff spatial angular frequency. The track irregularity of class 6 is used in this study for illustration purposes with  $k = 1$ ,  $A_r = 0.0339 \text{ cm}^2 \cdot \text{rad/m}$ , and  $\Omega_c = 0.8245 \text{ rad/m}$ . Notice that, as track irregularities are broadband, the behavior of the peaks of interest won't change substantially except their magnitude if a different type of irregularities is considered.

#### 4.2. Frequency response of coupled system

To facilitate mechanical analysis, the original coupled model can be decomposed into several subsystems, the vehicle, the contact springs, the irregularity, and the rail, as shown schematically in Fig. 7. The displacement response of the vehicle can be determined by the frequency-domain method

$$\mathbf{U} = -\mathbf{H}_v \mathbf{F} \quad (11)$$

where  $\mathbf{H}_v = (-\mathbf{m}\omega^2 + i\omega\mathbf{c} + \mathbf{k})^{-1}$  is defined as the frequency response function (FRF) matrix of the vehicle subsystem. It is noted that interactions between the wheels and the track occur at 4 DOFs. Therefore, the vehicle system can be reduced to 4 DOF by using the condensation technique. The response amplitudes of the wheels and the interaction forces are obtained by

$$\mathbf{U}_w = \mathbf{I}_T \mathbf{U} = \{U_{w1} \ U_{w2} \ U_{w3} \ U_{w4}\}^T \quad (12)$$

$$\mathbf{F}_w = \mathbf{I}_T \mathbf{F} = \{F_1 \ F_2 \ F_3 \ F_4\}^T \quad (13)$$

where  $\mathbf{I}_T$  is the transfer matrix for reducing the 10-DOF system to a 4-DOF one.

The response amplitudes of the wheels can then be derived from the interaction forces

$$\mathbf{U}_w = -\mathbf{H}_w \mathbf{F}_w \quad (14)$$

where the reduced FRF matrix of the wheels  $\mathbf{H}_w$  can be determined as  $\mathbf{H}_w = \mathbf{I}_T \mathbf{H}_v \mathbf{I}_T^T$  by using the condensation technique.

The relative compressions across the contact springs can be derived by

$$\mathbf{U}_c = \mathbf{H}_c \mathbf{F}_w \quad (15)$$

where  $\mathbf{H}_c$  is defined as the FRF matrix of the contact subsystem. As the four linearized contact springs are unconnected,  $\mathbf{H}_c$  is determined as a diagonal matrix, i.e.,  $\mathbf{H}_c = \text{diag}\{1/k_c \ 1/k_c \ 1/k_c \ 1/k_c\}$ .

As is demonstrated above, when the observation point moves with the vehicle, the response of the contact points on the track will be stationary and harmonic. Therefore, the frequency-domain method can be applied to obtain the response of the contact points on the track through

$$\mathbf{U}_t = \mathbf{H}_t \mathbf{F}_w \quad (16)$$

where  $\mathbf{H}_t$  is the FRF matrix of the track subsystem and, by means of the superposition principle, can be determined from the point and transfer receptances, i.e., Eq. (7),

$$\mathbf{H}_t = \begin{bmatrix} H(0) & H(2b) & H(2a) & H(2a+2b) \\ H(-2b) & H(0) & H(2a-2b) & H(2a) \\ H(-2a) & H(-2a+2b) & H(0) & H(2b) \\ H(-2a-2b) & H(-2a) & H(-2b) & H(0) \end{bmatrix} \quad (17)$$

The track irregularities are assumed to be a spatial stochastic process. If the running of the vehicle is taken into consideration, the irregularities under each contact point become temporal variables. To ensure the wheel-rail contact is maintained, the various displacements are related by

$$\mathbf{U}_w - \mathbf{U}_t + \mathbf{R}_w = \mathbf{U}_c \quad (18)$$

where  $\mathbf{R}_w$  is the amplitude vector of irregularities at certain frequency (positive for an asperity). Substituting Eq. (14)-(16) into Eq. (18), the interaction forces  $\mathbf{F}_w$  is obtained as

$$\mathbf{F}_w = (\mathbf{H}_w + \mathbf{H}_t + \mathbf{H}_c)^{-1} \mathbf{R}_w = \mathbf{K}_d \mathbf{R}_w \quad (19)$$

where  $\mathbf{K}_d = (\mathbf{H}_w + \mathbf{H}_t + \mathbf{H}_c)^{-1}$  is a dynamic stiffness matrix, the inverse of the combined receptance matrix, which converts spatial geometric irregularities into equivalent wheel-rail interaction forces. In the meantime, the displacement response of the contact points on the track can be easily obtained through Eq. (16) as  $\mathbf{U}_t = \mathbf{H}_t \mathbf{K}_d \mathbf{R}_w$ .

### 4.3. Response PSD

The spectral density matrix for the wheel-rail contact force  $\mathbf{S}_{f_w}$  and for the response of the contact points on the track  $\mathbf{S}_{u_t}$  can be then obtained as

$$\mathbf{S}_{f_w} = \lim_{T \rightarrow \infty} \frac{\mathbf{F}_w^* \mathbf{F}_w^T}{2T} = \mathbf{K}_d^* \mathbf{S}_r \mathbf{K}_d^T \quad (20)$$

$$\mathbf{S}_{u_t} = \lim_{T \rightarrow \infty} \frac{\mathbf{U}_t^* \mathbf{U}_t^T}{2T} = \mathbf{H}_t^* \mathbf{K}_d^* \mathbf{S}_r \mathbf{K}_d^T \mathbf{H}_t^T \quad (21)$$

where the superscript \* denotes the conjugate and superscript T denotes the transpose operation.  $\mathbf{S}_r$  is defined as the spectral density matrix for the irregularities of contact points given by

$$\mathbf{S}_r = \lim_{T \rightarrow \infty} \frac{\mathbf{R}_w^* \mathbf{R}_w^T}{2T} = \mathcal{B}(\omega, V) \frac{1}{V} S_r\left(\frac{\omega}{V}\right) \quad (22)$$

in which  $S_r(\Omega)$  is the spatial-PSD function of track irregularities in Eq. (10);  $\mathcal{B}(\omega, u)$  is a phase-lag matrix, describing relationships of time delay among the excitations. The use of the phase-lag matrix allows different types of excitations to be represented. For example, at low frequencies, excitations at each wheel can be regarded as strictly correlated, and  $\mathcal{B}(\omega, V)$  can be expressed as

$$\mathcal{B}(\omega, V) = \begin{bmatrix} 1 & e^{i\frac{\omega}{V}2b} & e^{i\frac{\omega}{V}2a} & e^{i\frac{\omega}{V}2(a+b)} \\ e^{-i\frac{\omega}{V}2b} & 1 & e^{i\frac{\omega}{V}2(a-b)} & e^{i\frac{\omega}{V}2a} \\ e^{-i\frac{\omega}{V}2a} & e^{-i\frac{\omega}{V}2(a-b)} & 1 & e^{i\frac{\omega}{V}2b} \\ e^{-i\frac{\omega}{V}2(a+b)} & e^{-i\frac{\omega}{V}2a} & e^{-i\frac{\omega}{V}2b} & 1 \end{bmatrix} \quad (23)$$

of which the derivation can be found in [36]. In contrast, at high frequencies an uncorrelated excitation model is more reasonable, for which  $\mathcal{B}(\omega, u)$  can be obtained as  $\mathcal{B}(\omega, V) = \text{diag}\{1 \ 1 \ 1 \ 1\}$ . For the active-passive wheel model which has been developed in [10], the irregularity excitation is only applied on one wheel at a time. If the first wheel is treated as the active wheel,  $\mathcal{B}(\omega, u)$  can be expressed as  $\mathcal{B}(\omega, V) = \text{diag}\{1 \ 0 \ 0 \ 0\}$ .

## 5. Mechanism Analysis

### 5.1. Multiple peaks in response PSD

The frequency-domain method presented in Section 4 is first applied to analyze the vibration of the train-track coupled system introduced in Fig. 6 with the uncorrelated irregularity excitations at four wheels. The PSDs of vertical contact forces from the first and second wheels are shown in Fig. 8 (a), for a passage speed of 40 m/s. Moreover, Fig. 8 (b) shows the PSDs of contact forces for a track coupled with four wheels with the irregularity excitation only on the third wheel. This model represents a pair of bogies at the adjacent ends of two vehicles, with  $b = 1.25$  m and  $c = 3.55$  m. In the latter case the

bogies and car body are omitted from the model; this only affects the results at frequencies below 10 Hz. As can be seen from Fig. 8, similar response peaks can be observed at frequencies above 200 Hz in the contact forces obtained from both models. The middle wheels (blue lines) present more peaks than the side wheels (red lines). These results broadly resemble the experimental results in Fig. 2, especially when the four adjacent wheels are included in the model. Notice that the discrepancies between the field test results and simulation results will be discussed in Section 5.4.

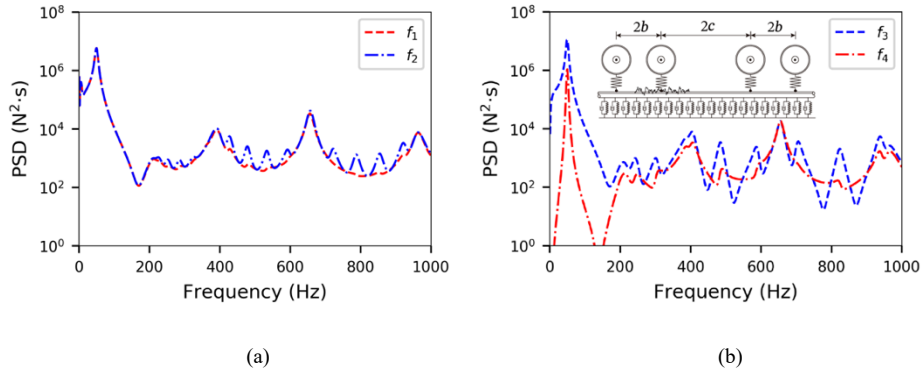


Fig. 8. PSD functions of wheel-rail contact forces for the system of: (a) a half vehicle on the rail subjected to uncorrelated irregularity excitations at all four wheels; (b) four wheels on the rail with track irregularity only on the third wheels.

## 5.2. Influence of two wheels on wheel-rail interactions

In order to investigate the multiple peaks observed both in the field measurement and the simulations in Fig. 8, a simplified model including active and passive wheel/rail interactions is applied in the following sections. The simplified model consists of an infinite continuously supported Timoshenko beam for the rail together with two longitudinally arranged wheels linked by a hinged massless bar, as shown in Fig. 9. Track irregularities are assumed to exist under the right-hand wheel (the active wheel), using the US FRA class 6 spectrum in Eq. (10), and the other wheel is excited only by the rail vibration; this is treated as the passive wheel. Responses of this simplified model can be easily calculated based on previous derivations in section 4, in which certain functions need to be adjusted and their expressions are given in Appendix A for the sake of brevity.

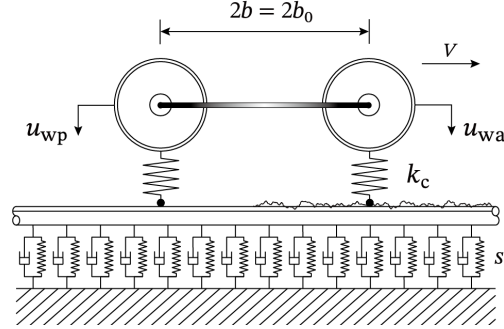


Fig. 9. An infinite Timoshenko beam model of the rail with two wheels linked by a hinged bar with irregularities only existing under the active wheel.

The response PSDs of the active and passive contact forces are presented in Fig. 10 (a), for a passage speed of 40 m/s. As a comparison, the response PSD of wheel-rail contact forces for a single wheel running on the rail at 40 m/s is shown in Fig. 10 (b).

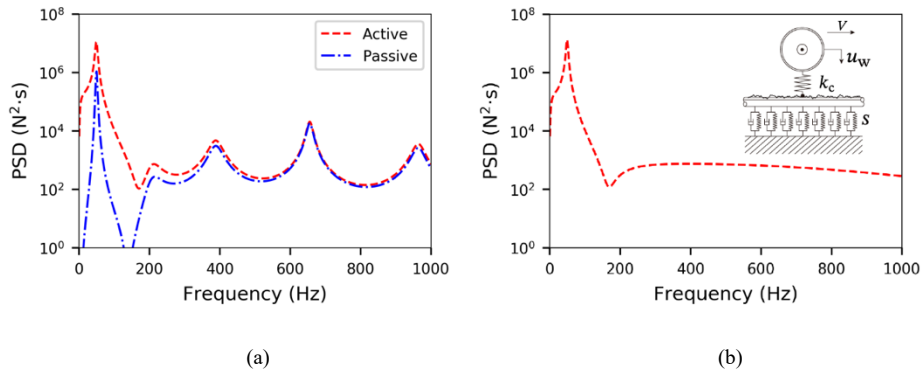


Fig. 10. PSD functions of wheel-rail contact forces for the system of (a) the active and passive wheels on the rail; (b) a single wheel on the rail.

Similar to Fig. 8, it can be observed from Fig. 10 (a) that, besides the original resonance peak around 50 Hz, there is a set of peaks at 400 Hz and above. In contrast, these additional peaks do not occur in Fig. 10 (b), with only the peak corresponding to the P2 resonance of the wheel on the rail appearing. Therefore, the effects of multiple wheels on the rail have changed the pattern of wheel/rail interactions, leading to multiple peaks in the response.

### 5.3. Contact force expressions

These multiple peaks can be explained from a mathematical perspective. Assume the active wheel is subjected to a particular component of track irregularities with a constant wavelength. Utilizing the frequency-domain method established above, the interaction forces  $\mathbf{F}_w = [F_a \ F_p]^T$  can be derived from Eq. (19), in which  $F_a$  represents contact forces of the active wheels and  $F_p$  for the passive wheels. Note that the irregularity under the passive wheels is zero, so the irregularity vector can be expressed as  $\mathbf{R}_w = [R \ 0]^T$ .

Besides, the FRF matrices of the subsystem are all second order matrices. The active and passive contact forces can then be determined by

$$F_a = \frac{\left[ H(0, \omega) + \frac{1}{k_c} - \frac{1}{m_w \omega^2} \right] R}{\left[ H(0, \omega) + \frac{1}{k_c} - \frac{1}{m_w \omega^2} \right]^2 - H(2b, \omega)H(-2b, \omega)} \quad (24)$$

$$F_p = \frac{-H(-2b, \omega)R}{\left[ H(0, \omega) + \frac{1}{k_c} - \frac{1}{m_w \omega^2} \right]^2 - H(2b, \omega)H(-2b, \omega)} \quad (25)$$

where the element  $H(\xi, \omega)$  represents the receptance of the rail, given by Eq. (7). It can be seen that the contact forces are complicated complex functions, especially as the rail receptance  $H(\xi, \omega)$  is a complex integral, but the contact force will reach a local maximum if the modulus of the denominator in Eq. (24) or Eq. (25) has a local minimum. Fig. 11 gives the modulus of the denominator in contact forces at different frequencies.

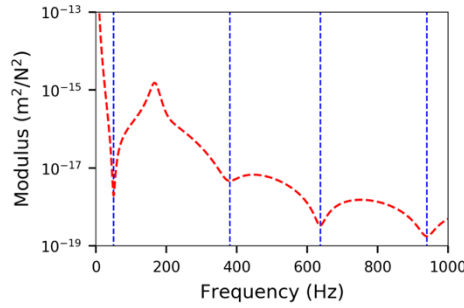


Fig. 11. The modulus of the denominator in contact force expressions at different frequencies.

As is expected, the curve has local minima at around 50 Hz, 380 Hz, 635 Hz and 950 Hz, exactly the places where the multiple peaks occur in Fig. 10 (a). This kind of explanation makes sense from a mathematical viewpoint, but it fails to provide an intuitive physical interpretation and still cannot answer the question why these functions have local extrema at certain frequencies.

#### 5.4. Explanation based on wave propagation theory

In fact, the vibration of the rail consists of waves, which propagate along the rail and can be reflected by the wheels; the responses are formed of the superposition of these waves. To show the wave propagation effect, a series of models are considered in which the wheelbase  $2b$  of a bogie is varied. Fig. 12 gives the PSDs of the active and passive contact forces and the phase differences between them. Results are shown for cases with  $b = 0.5b_0, b_0, 1.5b_0$  and  $2b_0$ , in which  $b_0$  is the original half wheelbase of 1.25 m.

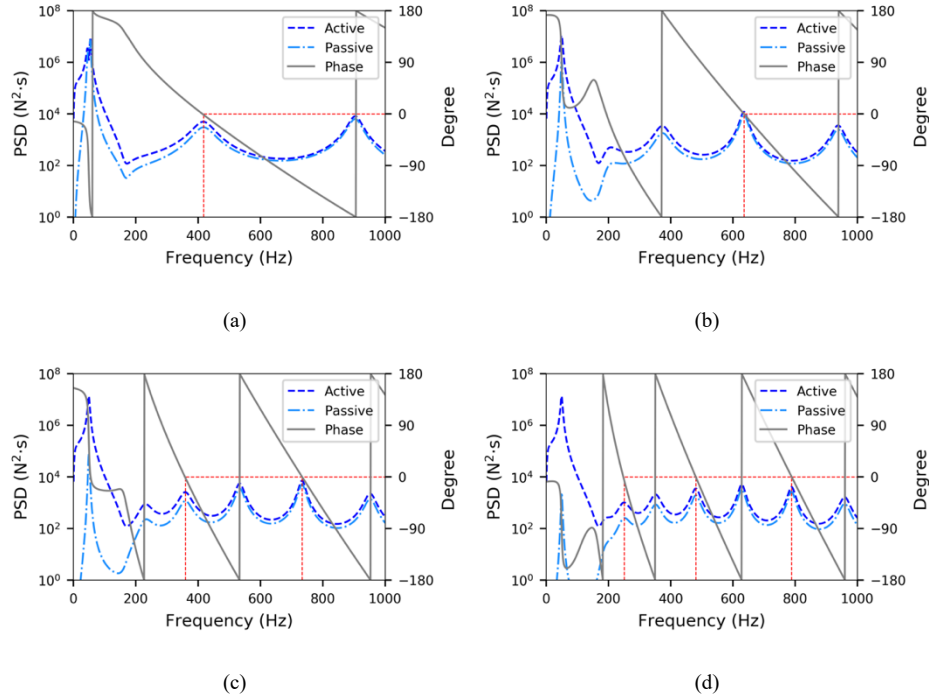


Fig. 12. PSDs and phase differences of the active and passive contact forces for wheelbase of (a)  $b = 0.5b_0$ ; (b)  $b = b_0$ ; (c)  $b = 1.5b_0$ ; (d)  $b = 2b_0$ .

These results show that, when the responses reach the local maxima, the two contact forces are either in phase or  $180^\circ$  out of phase, signifying intensification of the waves. For the active wheel, for example, the wave excited by the active wheel radiates outwards along the rail, and is partially reflected by the passive wheel. If the reflected wave is in phase with the irregularities, the excitation for the active wheel will be enhanced, and so will be the response.

In this case, the active wheel is initially excited by irregularities and generates the wheel-rail contact force  $F_{a1}$ , defined as the first order active contact force with a subscript 1 and derived as

$$F_{a1} = K_d R_0 \quad (26)$$

in which  $R_0$  is the irregularity (positive downward) and  $K_d$  is the dynamic stiffness function for a single wheel-rail contact

$$K_d = \frac{1}{-\frac{1}{m_w \omega^2} + H(0, \omega) + \frac{1}{k_c}} \quad (27)$$

in which  $H(0, \omega)$  is the point receptance of the rail at the contact point ( $\xi = 0$ ). It is worth pointing that, for frequencies between 100 and 1000 Hz,  $|H(0, \omega)|$  is much larger than the other two terms and therefore



$$K_d \approx \frac{1}{H(0, \omega)} \quad (28)$$

The incident wave  $w_i(\xi, t)$  excited by  $F_{a1}$  propagates (in the negative  $\xi$  direction) to the passive contact point, and the vibration of this point  $w_i(-2b, t)$  can be obtained from Eq. (26) by multiplying by a transfer receptance  $H(-2b, \omega)$

$$w_i(-2b, t) = H(-2b, \omega) F_{a1} \quad (29)$$

As discussed in Section 3, the transfer receptance at frequencies above 300 Hz is dominated by the  $k_2$  (or  $k_4$ ) component at sufficient distance from the excitation point. Therefore, by ignoring the rapidly decaying component ( $k_1$  term), from Eq. (7)  $H(-2b, \omega)$  can be simplified as

$$H(-2b, \omega) \approx i \frac{M(k_2)}{N'(k_2)} e^{ik_2 2b} \quad (30)$$

The vibration  $w_i(-2b, t)$  can be seen as an equivalent track irregularity that causes a secondary interaction force at the passive wheel. This can be written as

$$R_1 = w_i(-2b, t) = \eta_i R_0 \quad (31)$$

Here,  $\eta_i$  describes the changes of the magnitude and phase of  $R_1$  from the initial irregularity  $R_0$

$$\eta_i = \frac{R_1}{R_0} = H(-2b, \omega) K_d \approx \frac{H(-2b, \omega)}{H(0, \omega)} \quad (32)$$

The equivalent irregularity  $R_1$  will excite the passive wheel and generate a first order passive contact force  $F_{p1}$ . This is given by

$$F_{p1} = K_d R_1 \quad (33)$$

Comparing Eqs (26), (32) and (33) it can be seen that  $F_{p1} = \eta_i F_{a1}$ . The force  $F_{p1}$  will then excite a reflected wave  $w_r(\xi, t)$  in the rail which will propagate back to the active wheel. It will excite the active wheel and can again be seen as an equivalent irregularity  $R_2$ .  $R_2$  can be obtained as

$$R_2 = H(2b, \omega) F_{p1} = \eta_r R_0 \quad (34)$$

in which  $H(2b, \omega)$  is a transfer receptance at  $\xi = 2b$  and can be simplified as

$$H(2b, \omega) \approx -i \frac{M(k_4)}{N'(k_4)} e^{-ik_4 2b} \quad (35)$$

and  $\eta_r$  describes the changes of the magnitude and phase of  $R_2$  from the initial irregularity  $R_0$

$$\eta_r = \frac{R_2}{R_0} = H(2b, \omega) H(-2b, \omega) K_d^2 \quad (36)$$

In this process, the magnitude and phase of the reflection  $R_2$  generated from the initial irregularity  $R_0$  [26] undergo a series of changes

$$R_0 \xrightarrow{\times K_d} F_{a1} \xrightarrow{\times H(-2b, \omega)} R_1 \xrightarrow{\times K_d} F_{p1} \xrightarrow{\times H(2b, \omega)} R_2 \quad (37)$$

Fig. 13 depicts the process of wave generation, propagation, and reflection during wheel-rail interactions. After being excited by initial irregularities  $R_0$ , the incident wave  $w_i(\xi, t)$  propagates outward from the active contact point, and serves as an equivalent track irregularity  $R_1$  at the passive wheel. In the same way, the equivalent irregularity  $R_1$  excites a reflected wave  $w_r(\xi, t)$ , and it will propagate back to the active point as a reflection  $R_2$ . If the reflection  $R_2$  and the initial irregularity  $R_0$  are in phase,

$$\text{Arg}[\eta_r] = 2n\pi \quad (38)$$

for integer values of  $n$ , the excitation for the active wheel will be enhanced due to the constructive interference.

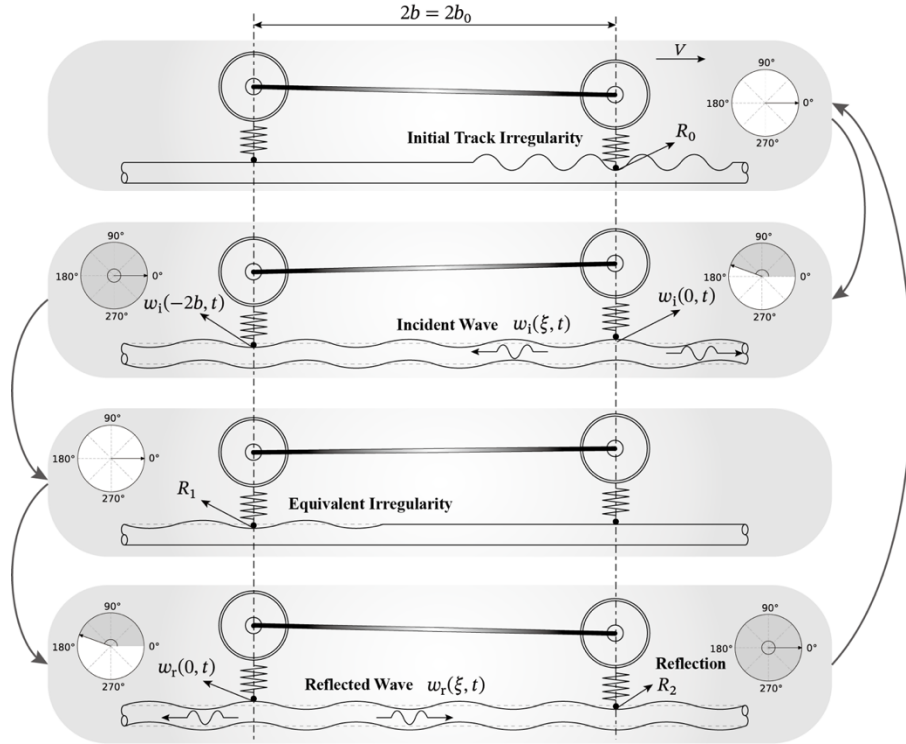


Fig. 13. The process of wave generation, propagation, and reflection during wheel-rail interactions.

It is noted that  $k_2$  is approximately equal to  $-k_4$  because the speed of bending waves is much greater than the train speed. In this case,  $H(2b, \omega)$  is approximately equal to  $H(-2b, \omega)$  and  $\eta_r \approx \eta_i^2$ . Therefore, Eq. (38) can be equivalently expressed as

$$\text{Arg}(\eta_i) = n\pi \quad (39)$$

Eq. (39) also represents the condition on the phase difference between  $F_{a1}$  and  $F_{p1}$  in the case of intensification. By substituting Eq. (32) and Eq. (7), the condition of wave intensification can be further evaluated as

$$\text{Arg} \left[ \frac{M(k_4)N'(k_3)}{M(k_3)N'(k_4) + M(k_4)N'(k_3)} \right] - \text{Re}(k_4)2b = n\pi \quad (40)$$

This qualitatively shows that the condition depends on the wheelbase and the wavenumbers of the rail. Notice that, as the wavenumbers are determined by roots of the quartic polynomial Eq. (5), which is also a function of frequency, it is possible to give a numerical solution of the condition for a specific case. Fig. 14 shows the magnitude and phase of  $\eta_i$  and  $\eta_r$  for wheelbase of  $b = b_0$ .

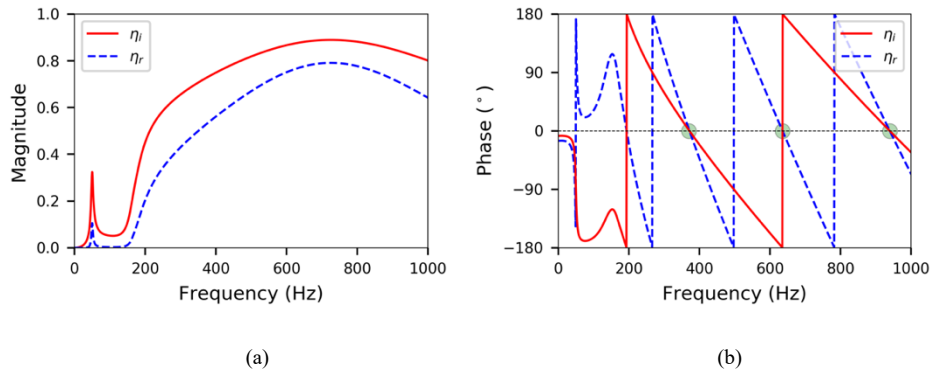


Fig. 14. The coefficients  $\eta_i$  and  $\eta_r$  for wheelbase of  $b = b_0$ : (a) magnitude; (b) phase.

It can be seen that the magnitudes of the two coefficients are both less than 1, due to the effect of wave attenuation and the influence of the wheel and contact receptances in  $K_d$ . The phase of  $\eta_i$  reaches 0 or  $\pi$  at around 380 Hz, 635 Hz and 950 Hz, where the phase of  $\eta_r$  is  $2\pi$ . This is consistent with the results in Fig. 12 (b) in which the peak in the contact forces occurs when the phase difference between them is either 0 or  $\pi$ .

Fig. 15 shows the phase changes of the intermediate variables from the initial irregularity to the reflection in the case of intensification at 635 Hz.

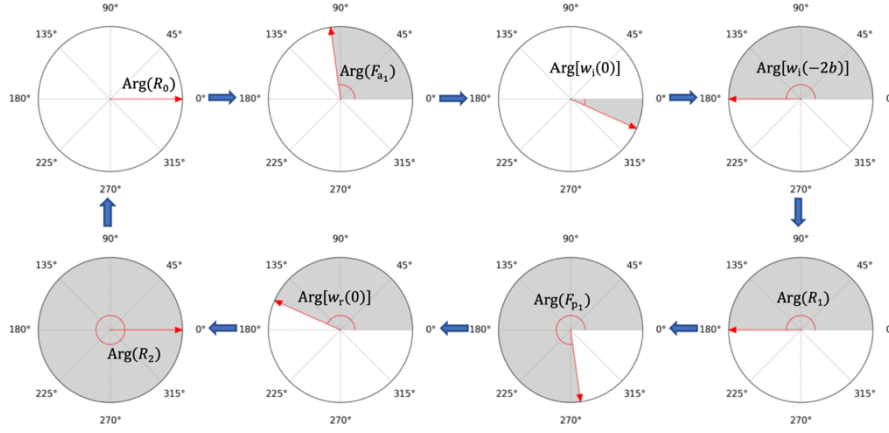


Fig. 15. The phase changes in the case of intensification between the initial irregularity and the reflection at 635 Hz.

The phase of the reflection returns to  $2\pi$ , and it will continue to propagate and get reflected between the two wheels. In fact, as long as the reflection  $R_2$  has the same phase as the initial irregularity, the excitation will be continuously intensified. Thus, the total equivalent irregularity becomes

$$R_{\text{total}} = \sum_{n=0}^{\infty} |\eta_r|^n R = \frac{R}{1 - |\eta_r|} \quad (41)$$

Fig. 14 (a) shows that  $|\eta_r|$  is larger than 0.6 at frequencies above 400 Hz, so  $R_{\text{total}}$  will be more than  $2.5R$  according to Eq. (41). This shows that wave interference will have a significant effect on the intensification of excitations. In particular,  $|\eta_r|$  reaches the peak (around 0.8) at 700 Hz, and  $R_{\text{total}}$  exceeds  $5R$  in this case. This explains that there is maximum amplification at the peak around 635 Hz, compared to other additional peaks in Fig. 12 (b).

As the number of wheels increases, there will be more reflected waves between multiple wheels, leading to a more complicated condition of wave intensification and an increase in consequent peaks in the response. This can be justified by comparing the two-wheel results of Fig. 10 to the four-wheel results of Fig. 8, and also the field test results of a three-vehicle train in Fig. 2 (b). Notice that, the field measurement was conducted at a fixed point on the rail, and there may be additional peak energies in excitations at certain wavelengths, e.g., due to wheel flats or combined irregularities of wheel and rail, etc. These facts may lead to unexpected changes in the peak patterns of the field test results, e.g., peaks from 200 Hz to 400 Hz in Fig. 2 (b).

The wave interference phenomenon is insignificant at low frequencies because waves are strongly attenuated when travelling in the rail in this frequency region.[17] According to Fig. 4 (b), the decay rates at frequencies below 200 Hz are above 10 dB/m. Therefore, the wheel-rail interactions at low frequencies are not affected by the wave reflections.

## 6. Influence of Load Speed on Wheel-rail Interactions

Usually, a moving irregularity model is applied to solve train-track coupled dynamics in the frequency domain, in which the train is assumed to be stationary and irregularities are pulled between wheels and the rail as a relative excitation. As discussed in Section 3, the wavelength of the wave propagating in the same direction as the moving excitation is shorter than that propagating in the opposite direction due to effects of the load motion on the poles, namely the Doppler effect. The difference between the wavelengths of the waves heading in each direction gradually increases as the load speed increases.

In this section it is investigated whether the load speed has an effect on the peaks in the PSD of wheel-rail contact forces. Different values of pad stiffness are also considered. The PSDs of the wheel-rail contact forces are calculated by using the moving load approach and the moving irregularity approach and compared for different fastener stiffness and train speeds. The investigation is still based on the simplified model shown in Fig. 9 with  $b = 1.25$  m.

Fig. 16 shows the force PSD for two values of pad stiffness (10 MN/m and 40 MN/m) for a fastener spacing of 0.6 m, and a train speed of 100 m/s; Fig. 17 shows results for two higher values of train speed (200 m/s and 300 m/s) with the pad stiffness of 40 MN/m for a fastener spacing of 0.6 m. Notice that these high speeds are considered in order to illustrate Doppler effect on wheel-rail interactions despite their impracticability for the current trains in operation.

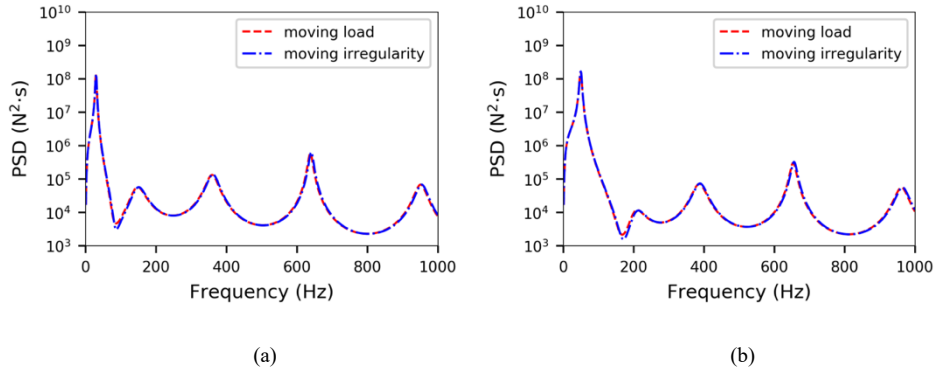


Fig. 16. PSDs of the active contact forces at  $V = 100$  m/s by using the moving load model (red line) and the moving irregularity model (blue line) with pad stiffness of (a) 10 MN/m; (b) 40 MN/m.

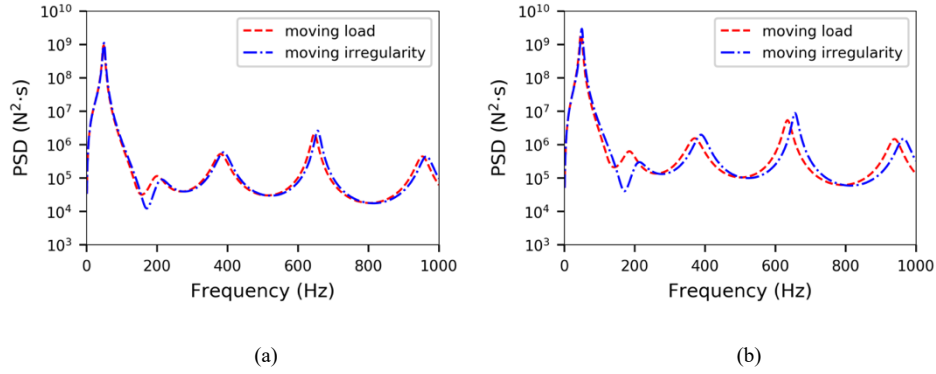


Fig. 17. PSDs of the active contact forces with pad stiffness of 40 MN/m at a fastener spacing of 0.6 m by using the moving load model (red line) and the moving irregularity model (blue line) at the train speed of (a) 200 m/s; (b) 300 m/s.

It can be seen from Fig. 16 that differences between the contact forces obtained using the moving load model and the moving irregularity model are small, showing that Doppler effect has little influence on wheel-rail interactions for these cases. In contrast, as is shown in Fig. 17, the difference is slightly increased with the increase of train speed, and Doppler effect can be observed for a train speed of 300 m/s. These peaks for the moving load model are seen to move to the lower frequency range, compared to that of the moving irregularity model. It is noted that the shift in the peaks in the upper frequency region is greater than in the low frequency region. However, since practical train speeds are usually below 100 m/s, these results show that the moving irregularity model is sufficient in most practical cases.

Comparing the cases for different pad stiffness in Fig. 16, the position of the peaks is unaffected but the height of the peaks is increased for the softer rail pads. This is related to the lower decay rate that such a track exhibits.

## 7. Conclusions

This study has investigated the phenomenon and the mechanism of multiple peaks in the high-frequency rail vibration spectra. A frequency-domain method has been adopted to calculate the PSD responses of the train-track coupled system excited by multi-wheel moving excitations and stochastic irregularities. The track is modelled as an infinite Timoshenko beam with continuous supports. Based on the residue theorem, the point and transfer receptances of the rail are explicitly determined using a Fourier transform-based method.

The results from the train-track dynamic interaction model show the multiple peaks in the responses of the system, around 400 Hz to 1000 Hz, occur with the presence of multiple wheelsets on the rail. Based on the wave propagation theory, it is found that the multiple peaks occur when the bending rail waves reflected from multiple wheels on the rail are exactly in phase with the initial irregularity. This suggests the high-frequency rail response to multiple wheels cannot be simply treated as the combination of individual responses to

a series of single wheels by using superposition principle, as conventionally done.[10] Instead, the wave interference between multiple wheels shall be considered. And the consequent peak responses would be responsible for typical wear patterns on the railhead.[17]

Although the model has been based on a moving excitation, the influence of the Doppler effect on the wheel-rail contact forces is found to be small for a practical range of parameter values. Where the train speed is 100 m/s or below, the effect of load motion is insignificant, and a moving irregularity model can be used to solve train-track coupled dynamics.

### Acknowledgements

The study was supported by the National Natural Science Foundation of China (grant numbers 52278520, 51978527 and 52178432), and the State Key Laboratory of Disaster Reduction in Civil Engineering (grant number SLDRCE19-A-04) and the China Scholarship Council (No. 202106260170).

### Appendix A

$$\mathbf{H}_w = -\text{diag}\left\{\frac{1}{m_w\omega^2} \quad \frac{1}{m_w\omega^2}\right\} \quad (\text{A1})$$

$$\mathbf{H}_c = \text{diag}\left\{\frac{1}{k_c} \quad \frac{1}{k_c}\right\} \quad (\text{A2})$$

$$\mathbf{H}_t = \begin{bmatrix} H(0) & H(2b) \\ H(-2b) & H(0) \end{bmatrix} \quad (\text{A3})$$

$$\mathbf{B}(\omega, V) = \text{diag}\{1 \quad 0\} \quad (\text{A4})$$

### References

- [1] Y.B. Yang, J.D. Yau, Vertical and pitching resonance of train cars moving over a series of simple beams, *J. Sound Vibr.*, 337 (2015) 135-149.
- [2] Q. Zeng, Y.B. Yang, E.G. Dimitrakopoulos, Dynamic response of high speed vehicles and sustaining curved bridges under conditions of resonance, *Engineering Structures*, 114 (2016) 61-74.
- [3] Y.B. Yang, J.D. Yau, Resonance of high-speed trains moving over a series of simple or continuous beams with non-ballasted tracks, *Engineering Structures*, 143 (2017) 295-305.
- [4] Y.-S. Wu, Y.-B. Yang, J.-D. Yau, Three-dimensional analysis of train-rail-bridge interaction problems, *Veh. Syst. Dyn.*, 36 (2001) 1-35.
- [5] Y.-S. Wu, Y.-B. Yang, Steady-state response and riding comfort of trains moving over a series of simply supported bridges, *Engineering Structures*, 25 (2003) 251-265.
- [6] H.H. Hung, G.H. Chen, Y.B. Yang, Effect of railway roughness on soil vibrations due to moving trains by 2.5d finite/infinite element approach, *Engineering Structures*, 57 (2013) 254-266.
- [7] Y.-B. Yang, J. Yau, Z. Yao, Y. Wu, *Vehicle-bridge interaction dynamics: With applications to high-speed railways*, World Scientific, 2004.
- [8] Y.B. Yang, C.W. Lin, *Vehicle-bridge interaction dynamics and potential applications*, *J. Sound Vibr.*, 284 (2005) 205-226.

- [9] Y.B. Yang, C.L. Lin, J.D. Yau, D.W. Chang, Mechanism of resonance and cancellation for train-induced vibrations on bridges with elastic bearings, *J. Sound Vibr.*, 269 (2004) 345-360.
- [10] T.X. Wu, D.J. Thompson, Vibration analysis of railway track with multiple wheels on the rail, *J. Sound Vibr.*, 239 (2001) 69-97.
- [11] Y. Yang, B. Zhang, T. Wang, H. Xu, Y. Wu, Two-axle test vehicle for bridges: Theory and applications, *International Journal of Mechanical Sciences*, 152 (2019) 51-62.
- [12] M. Sun, X.S. Fang, D.X. Mao, X. Wang, Y. Li, Broadband acoustic ventilation barriers, *Phys. Rev. Appl.*, 13 (2020) 8.
- [13] X. Wang, D. Mao, W. Yu, Z. Jiang, Acoustic performance of balconies having inhomogeneous ceiling surfaces on a roadside building facade, *Building and Environment*, 93 (2015) 1-8.
- [14] A. Igeland, Railhead corrugation growth explained by dynamic interaction between track and bogie wheelsets, *Proceedings of the Institution of Mechanical Engineers Part F-Journal of Rail and Rapid Transit*, 210 (1996) 11-20.
- [15] G. Fang, Y. Wang, Z. Peng, T. Wu, Theoretical investigation into the formation mechanism and mitigation measures of short pitch rail corrugation in resilient tracks of metros, *Proceedings of the Institution of Mechanical Engineers, Part F: Journal of Rail and Rapid Transit*, 232 (2018) 2260-2271.
- [16] T. Wu, D. Thompson, The effects on railway rolling noise of wave reflections in the rail and support stiffening due to the presence of multiple wheels, *Applied Acoustics*, 62 (2001) 1249-1266.
- [17] T. Wu, D. Thompson, Behaviour of the normal contact force under multiple wheel/rail interaction, *Veh. Syst. Dyn.*, 37 (2002) 157-174.
- [18] B. Ding, G. Squicciarini, D. Thompson, Effect of rail dynamics on curve squeal under constant friction conditions, *J. Sound Vibr.*, 442 (2019) 183-199.
- [19] X. Sheng, T. Zhong, Y. Li, Vibration and sound radiation of slab high-speed railway tracks subject to a moving harmonic load, *J. Sound Vibr.*, 395 (2017) 160-186.
- [20] K.L. Knothe, S.L. Grassie, Modeling of railway track and vehicle track interaction at high-frequencies, *Veh. Syst. Dyn.*, 22 (1993) 209-262.
- [21] X. Sheng, C.J.C. Jones, D.J. Thompson, Responses of infinite periodic structures to moving or stationary harmonic loads, *J. Sound Vibr.*, 282 (2005) 125-149.
- [22] X. Sheng, M.H. Li, Propagation constants of railway tracks as a periodic structure, *J. Sound Vibr.*, 299 (2007) 1114-1123.
- [23] J.C.O. Nielsen, A. Igeland, Vertical dynamic interaction between train and track - influence of wheel and track imperfections, *J. Sound Vibr.*, 187 (1995) 825-839.
- [24] X. Sheng, Generalization of the fourier transform-based method for calculating the response of a periodic railway track subject to a moving harmonic load, *Journal of Modern Transportation*, 23 (2015) 12-29.
- [25] T.X. Wu, Y.R. Wang, Modeling of wheel-track interaction with rail vibration damper and its application for suppressing short pitch rail corrugation, in: *Noise and vibration mitigation for rail transportation systems*, Springer, 2015, pp. 361-368.
- [26] T. Wu, D. Thompson, An investigation into rail corrugation due to micro-slip under multiple wheel/rail interactions, *Wear*, 258 (2005) 1115-1125.
- [27] D. Thompson, *Railway noise and vibration: Mechanisms, modelling and means of control*, Elsevier, Oxford, 2008.
- [28] Q. Li, D.J. Wu, Analysis of the dominant vibration frequencies of rail bridges for structure-borne noise using a power flow method, *J. Sound Vibr.*, 332 (2013) 4153-4163.
- [29] S.L. Grassie, R.W. Gregory, D. Harrison, K.L. Johnson, The dynamic response of railway track to high frequency vertical excitation, *Journal of Mechanical Engineering Science*, 24 (1982) 77-90.



- [30] J. Egana, J. Vinolas, M. Seco, Investigation of the influence of rail pad stiffness on rail corrugation on a transit system, *Wear*, 261 (2006) 216-224.
- [31] H. Ilias, The influence of railpad stiffness on wheelset/track interaction and corrugation growth, *J. Sound Vibr.*, 227 (1999) 935-948.
- [32] Q. Li, D.J. Thompson, Prediction of rail and bridge noise arising from concrete railway viaducts by using a multilayer rail fastener model and a wavenumber domain method, *Proceedings of the Institution of Mechanical Engineers, Part F: Journal of Rail and Rapid Transit*, 232 (2018) 1326-1346.
- [33] T. Mazilu, Prediction of the interaction between a simple moving vehicle and an infinite periodically supported rail - green's functions approach, *Veh. Syst. Dyn.*, 48 (2010) 1021-1042.
- [34] S. Lei, Y. Ge, Q. Li, D.J. Thompson, Frequency-domain method for non-stationary stochastic vibrations of train-bridge coupled system with time-varying characteristics, *Mech. Syst. Signal Proc.*, 183 (2023) 109637.
- [35] V. Garg, R.V. Dukkipati, *Dynamics of railway vehicle systems*, Elsevier, Toronto, 2012.
- [36] S.M. Lei, Y.J. Ge, Q. Li, Effect and its mechanism of spatial coherence of track irregularity on dynamic responses of railway vehicles, *Mech. Syst. Signal Proc.*, 145 (2020) 21.